Analysis and Results of the TOPSAR Experiments in Southern Italy

G. Alberti, S. Vetrella

CO.RI.S.T.A.
Piazzale V. Tecchio, 80 - 80125 Napoli, Italy

A. Moccia, S. Ponte

Faculty of Engineering, University of Naples "Federico II"
Piazzale V. Tecchio, 80 - 80125 Napoli, Italy

ABSTRACT

This paper presents the analysis of the C-band cross-track interferometric data (XTI) acquired during the MAC Europe 1991 Campaign over the Matera test site (Southern Italy). Passive and active calibrators were deployed over a homogeneous background, and a ground truth data collection campaign was carried out simultaneous with the flight. The raw data, gathered by the TOPSAR instrument on-board the NASA/JPL DC-8 aircraft, have been compressed with a range-Doppler SAR processor which takes range migration and antenna squint into account. The resulting interferogram has been obtained after co-registration performed by using 1D cross-correlation techniques. The airplane attitude angles, recorded by the navigation system, have been used to derive the baseline time variation, necessary for the 2π phase unwrapping procedure. Assuming unperturbed aircaft translational motion, the ± 0.2 mm accuracy on the estimate of the baseline components gave a theoretical rms error on the estimate of the height of each imaged pixel of ± 2.5 m for extended targets, and ± 4.5 m for point targets. Finally, the computed terrain elevation has been compared with the 1:25,000 scale digitised contour levels of the Istituto Geografico Militare Italiano (IGMI), in order to assess the height accuracy of the system. The root-mean-square errors on the height estimate have been found to be ± 15 m for point targets, and ± 8 m for extended targets.

INTRODUCTION

The extraction of topographic data by means of SAR interferometry has been successfully demonstrated in recent years. High-resolution terrain elevation maps have been obtained either by analysing existing spaceborne and airborne systems, capable of producing multiple-pass interferometric pairs (Gabriel and Goldstein 1988 for SIR-B, Prati *et al.* 1990 for Seasat, Gray and Farris-Manning 1993 for the CCRS SAR-580), or by means of two antennas mounted on the same platform (Graham 1974 for the Goodyear instrument, Zebker and Goldstein 1986 for the NASA CV-990 radar, Madsen *et al.* 1993a for TOPSAR). The TOPSAR instrument (Zebker *et al.* 1992), which is the interferometric addition to the NASA DC-8 Airborne SAR (AIRSAR), uses the single-pass approach, in order to overcome surface temporal decorrelation, which is a common phenomenon observed in multiple-track spaceborne SAR interferometry. In this case, the knowledge of the aircraft attitude is mandatory to optimise the overall performance and keep the system below the project specifications on the accuracy of the height estimate.

During the MAC Europe 1991 multisensor airborne campaign, sponsored by NASA, ESA, CEC, DLR, ASI, CNES, BNSC and ASA, cross-track interferometric (XTI) data were acquired over several test-sites, in order to verify the TOPSAR capability of delivering Digital Elevation Models (DEMs) at great height accuracy and little spatial resolution. The authors focused their attention on Matera test-site (Basilicata, Southern Italy), where a set of active and passive calibration devices were deployed over a flat, homogeneous background, and an extensive ground truth campaign was performed in conjunction with the flight date (June 25th, 1991). This paper presents the data analysis and the main results obtained from the interferometric processing developed by the Italian Consortium of Research on Advanced Remote Sensors (CO.RI.S.T.A.), in co-operation with the University of Naples, Italy. After a short description of the campaign, we present the main aspects of the coherent raw data focusing and the interferometric processing applied to obtain a DEM. In particular, the co-registration technique and the main considerations about the baseline estimation procedure and the related accuracy on the baseline components are outlined. The two-dimensional phase unwrapping
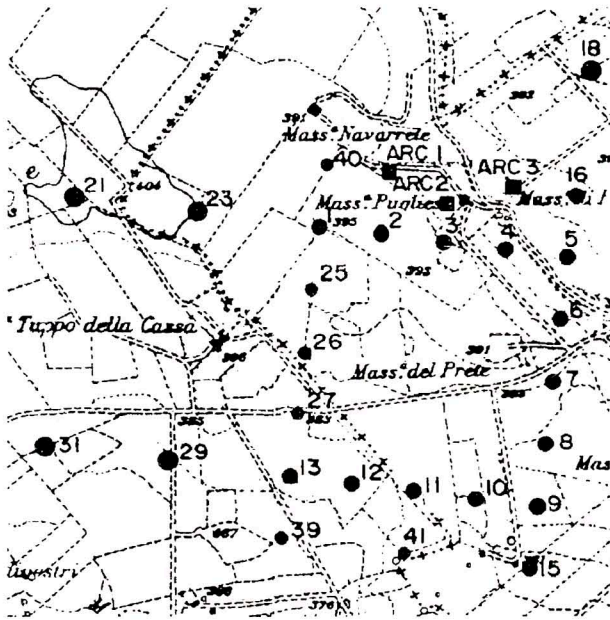
Fig. 1 - Deployment scheme of active and passive calibrators.

algorithm is summarised, and a thorough error budget on the height estimate for both point and extended targets is carried out. Successively, the topographic mapping technique is verified by comparing the radar-derived DEM with the 1:25,000 scale digitised height points of the Italian Military Geographic Institute (IGMI), and characterising the rms difference between the heights for some deployed point targets as well as for some known extended targets in the imaged scene. Finally, some considerations on further developments and future research activity are presented.

1. 1991 CAMPAIGN

On June 25, 1991, the TOPSAR instrument covered five times, with three descending and two ascending flights, the Italian Matera test-site, gathering C-band cross-track interferometric data. The imaged area extends over about 120 km^2, and consists of prevailingly bare soil, well suited for sensor system evaluation, with slight changes of terrain height (50 m peak-to-peak, 15 m average). Ancillary ground information was collected by carrying out a simultaneous ground truth campaign, consisting of the classification of 50 sample areas and to the evaluation of texture, soil moisture content and surface roughness on sample points close to the location of 26 calibration devices with different Radar Cross-Sections (RCS) (CO.RI.S.T.A. 1991). The point targets were three Active Radar Calibrators (ARCs), jointly developed by CO.RI.S.T.A. and Polytechnic of Bari, Italy, and 23 triangular trihedral Corner Reflectors (CRs), subdivided in 15, 5 and 3 with leg lengths of 95, 180 and 70 cm respectively. Figure 1 shows the deployment scheme of CRs

and ARCs on the test site, superimposed on the IGMI map of the area (1:25,000 scale). The calibration devices are positioned on two parallel lines in the horizontal (ground range) direction at a distance of 800 m with a spacing of 200 m between two successive CRs, to avoid coupling effects. All the point targets were deployed on a homogeneous background and positioned with electronic stadimeters and theodolites. The mean height of the calibrators' area was 390 m.

2. DATA ANALYSIS AND IMAGE PROCESSING

Table 1 lists the main TOPSAR radar system parameters involved in raw data focusing (Zebker *et al.* 1992). We processed a frame of 16384 lines of 1350 complex range samples per line, centred on the calibrators' region, and the total imaged area extends over about 6x4.5 km^2. The data compression has been performed by means of a range-Doppler SAR processor which includes range migration compensation and antenna squint correction. In the pre-processing phase, preliminary to the range compression, we have estimated from the raw data the amplitude of the calibration tone (commonly referred to as *caltone*) injected into the receiver chain and located just beyond the upper band edge of the chirp bandwidth, in order to remove the channel imbalance. Fig. 2 depicts the range spectrum of a line with its caltone: for the XTI operation mode, the calibration frequency is 5266.40625 MHz, and after down-conversion, i. e. subtraction of the 5310.0 MHz reference frequency, it is located at 43.59375 MHz. The caltone level was estimated from the range spectrum of each line, by extracting the amplitude of the Discrete Fourier Transform (DFT) coefficient corresponding to the caltone level, and successively subtracting the out-of-band noise level,

Table 1 - TOPSAR main radar system parameters.

|	
Frequency	5.2873 GHz (C-band)
Wavelength, λ	5.67 cm
Antenna length	1.6 m
Baseline length, B	2.583 m
Baseline tilt angle, ξ	62.77°
Aircraft speed, v	214.4 m/s
Side-looking angles, ϑ	45° (nominal); 30°-60°
Nominal altitude, H	9 km
Swath width	4630 m (slant range)
Slant range	11200 m (ϑ=45°)
Ground range resolution, ρ_{GR}	5.30 m
Slant range resolution, ρ_{SR}	3.75 m
Azimuth resolution, ρ_{AZ}	0.8 m (1 look)
Chirp bandwidth	40 MHz
Pulse length	5.0 µs
Sampling frequency	90 MHz
SNR (distributed targets)	13 dB
SNR (point targets)	18 dB
PRF	567 Hz
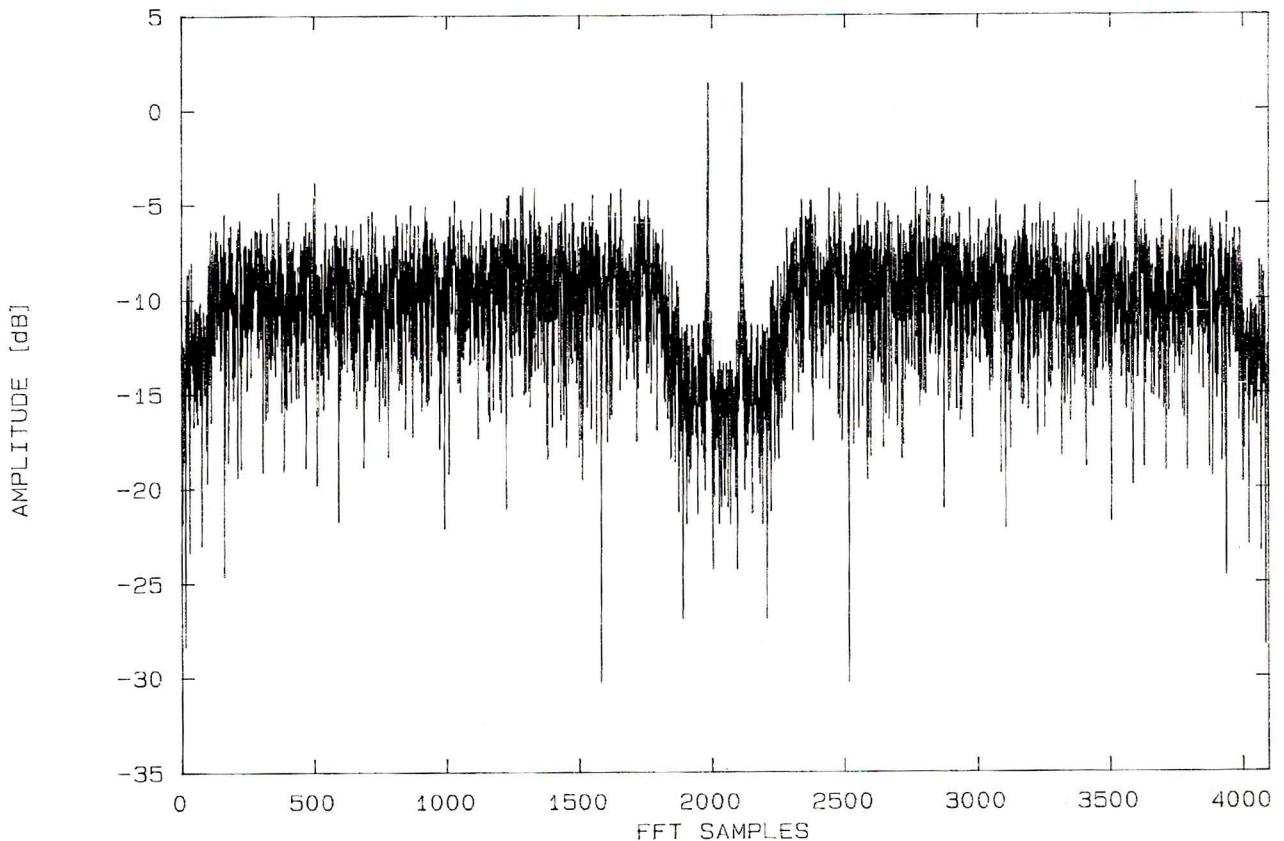
Fig. 2 - Range spectrum of the transmitting/receiving channel. On the upper side of the chirp band, the caltone level is visible.

derived from the amplitude-averaging of several adjacent frequency samples on the upper band side of the caltone position. After pre-processing, the range compression of the raw data has been obtained by applying a reference function which emulates the Digital Chirp Generator (DCG) implemented in the SAR system, that is, with a stair-step approximation of the linear frequency sweep and, consequently, with a locally linear synthesis of the quadratic phase of the FM chirp. A Hamming weighting has been used to reduce range sidelobes.

A range migration analysis has been conducted on the responses of the range-compressed calibrators. After 64-times oversampling by FFT techniques the range lines of the image subset containing the visible "stripe" of the CR (or ARC), the amplitude and position of the mainlobe peak value have been plotted as a function of the azimuth station (Fig. 3). In Fig. 3 the effect of the antenna azimuth pattern is clearly visible. A forward squint of the two antennas can be observed, whereas the slightly different shape of the range history of the same CR as seen by the antennas indicates the existence of a relative squint as well. The total change of range during the synthetic-aperture formation time, i. e. the range migration DR, has been found from the

above analysis to be two pixels, after normalisation with respect to the slant range resolution r_{sr}, and the range walk DR_{rw} (that is, the linear term of the Taylor's expansion of R(t) around R_0, the slant range at the closest approach) has been 68 m, depending on the slant range. These values are in agreement with the theoretical ones, given respectively by (Curlander and McDonough 1991):

$$\frac{|\Delta R|}{\rho_{sr}} = \frac{1}{\rho_{sr}} (|\Delta R_{rw}| + \Delta R_{rc}) =$$

$$= \frac{\lambda R_0}{4 \rho_{az} \rho_{sr}} \left(|\sin \vartheta_s| + \frac{\lambda}{4 \rho_{az}} \right) \quad \Delta R_{rw} = \frac{\lambda R_0}{4 \rho_{az}} \sin \vartheta_s$$

where ΔR_{rc} is the quadratic term of the Taylor's expansion (the range curvature), λ is the wavelength, ρ_{az} is the theoretical azimuth resolution, ϑ_s is the antenna squint angle with respect to the nominal flight path, evaluated as it will be shown later.

The corner-turned range-compressed data have been azimuth-processed in the frequency domain, estimating the Doppler centroid frequency with standard clutterlock techniques (Li *et al*. 1985). Fig. 4 shows the azimuth spectra for
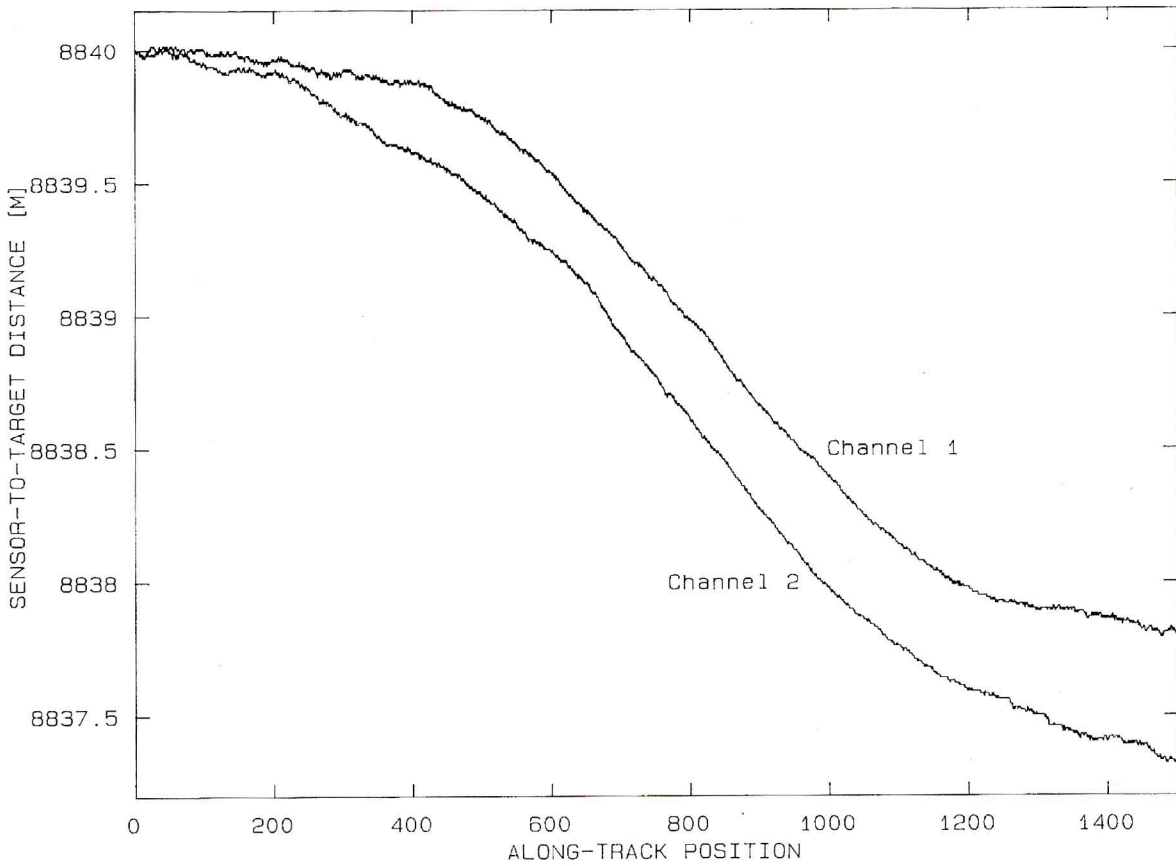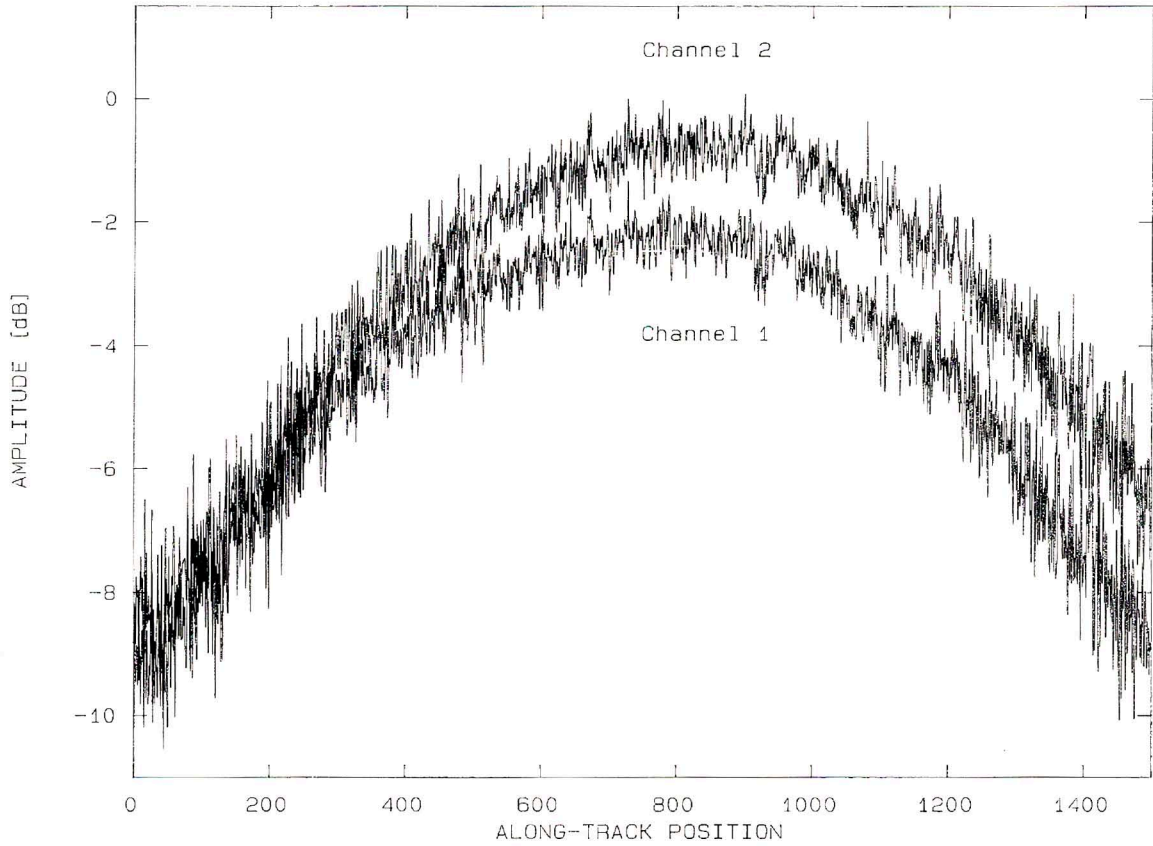
Fig. 3 - Range migration analysis: (a) Amplitude of the peak value of the mainlobe in the 64-times oversampled range-compressed image, as a function of the azimuth position; (b) slant range to the target during the antenna formation time.
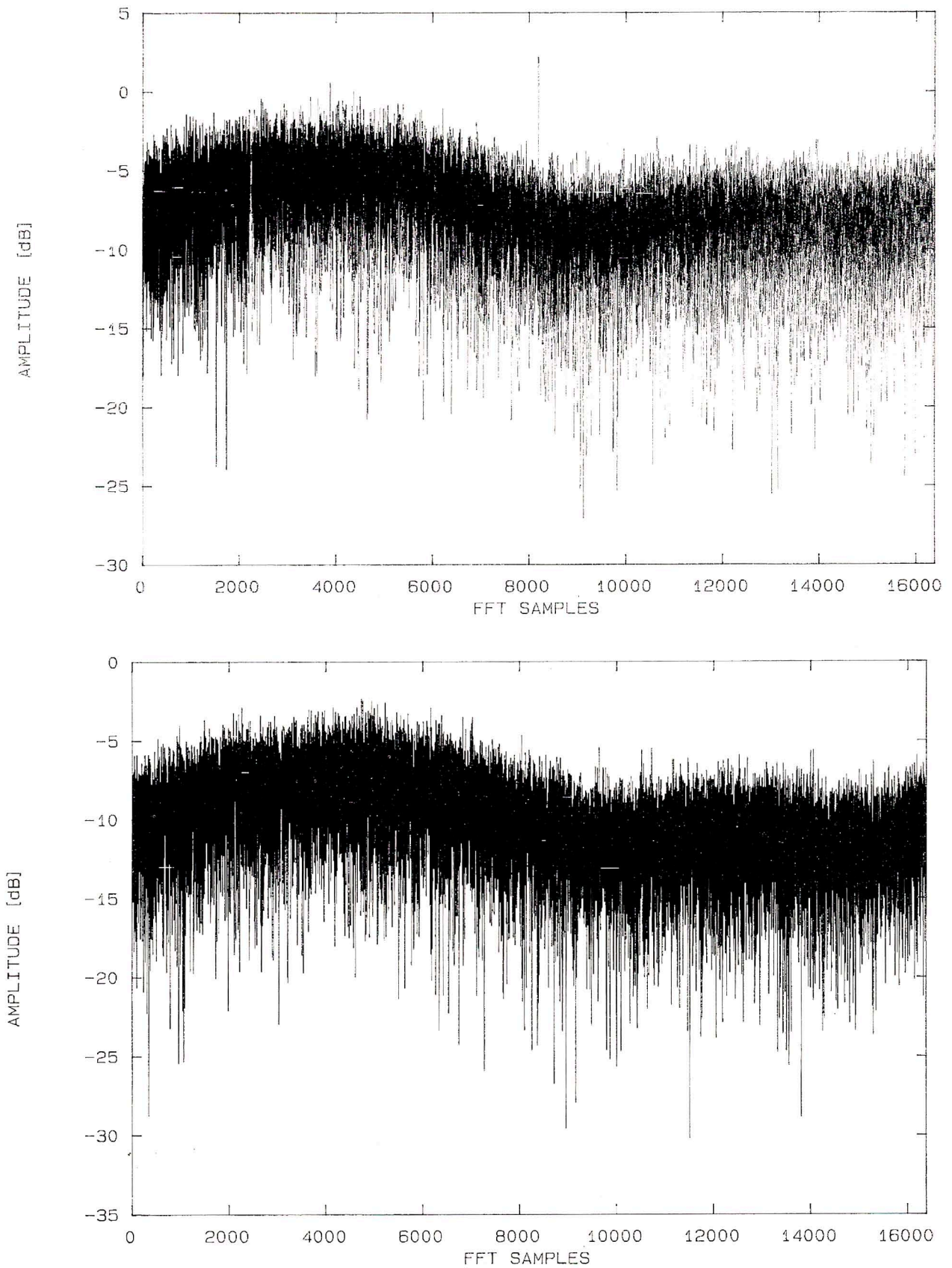
Fig. 4 - Azimuth spectra of the two channels. Note the two different Doppler centroid frequencies (-132.5 Hz for channel 1, tx/rx (a); -140 Hz for channel 2, rx (b)).
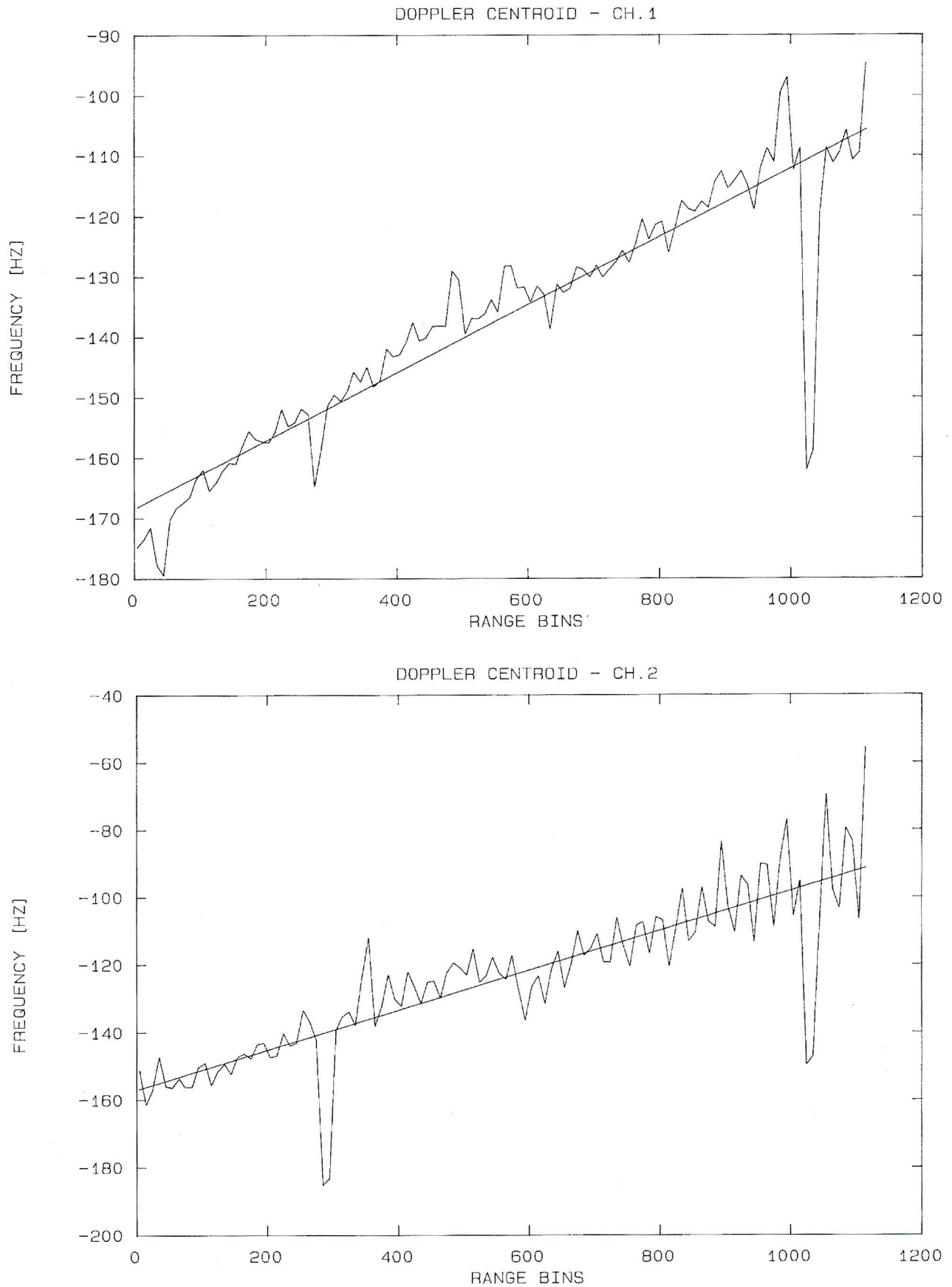
Fig. 5 - *Doppler centroid frequency computed by the clutterlock algorithm, and its linear least-squares approximations for channel 1 (a) and channel 2 (b) as a function of range.*

the two channels. The squint angles of the two antennas, $\vartheta_{s,1}$ and $\vartheta_{s,2}$, have been derived from the clutterlock estimate of the Doppler centroid, f_{DC}, with the formula:

$$\vartheta_{s,i} = \sin^{-1}\left(\frac{\lambda f_{DC,i}}{2\upsilon}\right), \quad i = 1,2$$

where υ is the aircraft speed. The estimated relative squint of the antennas is below 0.2 degrees. Due to the different values of f_{DC}, we applied different azimuth reference functions for the two channels, updating the filter parameters each processed line. In order to account for the Doppler centroid variation from near to far range, a linear least-squares approximation has been used to calculate the correct azimuth filter parameters. In Fig. 5, f_{DC} as a function of range bin is shown for both channels, together with the approximating line.

The range migration correction has been performed in the frequency domain, reallocating the complex DFT coefficients along lines parallel to the azimuth direction. The adopted algorithm is based on an 8-points cubic B-spline interpolation, and takes the aforementioned Doppler frequency variation into account. Due to the antennas' squint, the Doppler frequency variation is different in the two images (see Fig. 5). Since the processor does not create the images in the zero Doppler geometry, it is necessary to "realign" geometrically the contributions of the antennas and to correct the residual phase term. This is performed during the next step of the processing, simultaneously with the geometric registration of the images forming the interferometric pair. A Hamming weighting has been applied to the reference function. No multi-look algorithm has been performed before forming the interferogram.

A set of standard image quality tests have been carried out in order to validate the processor performance. We evaluated the one-dimensional ground range and azimuth resolutions, the Integrated Sidelobe Ratio (ISLR) and the Peak Sidelobe Ratio (PSLR) on the point target responses (JPL SIR-C Team et al. 1990, Moccia et al. 1991), finding a mean broadening factor of 5% in ground range, and about 15% in azimuth. We plan to improve the resolution values by implementing motion compensation algorithms. The mean value of the SNR for point targets has been found to be 18 dB.

3. INTERFEROMETRIC PROCESSING: CO-REGISTRATION, BASELINE ESTIMATION AND PHASE UNWRAPPING

3.1 Geometric registration

The aforementioned differences of the Doppler centroid frequencies for the two antennas caused a relative azimuth displacement in the final images, making therefore necessary the use of co-registration techniques. To this end, we applied a one-dimensional cross-correlation method. The cross-correlation function of the azimuth pixel amplitudes was oversampled by cubic B-spline techniques up to one tenth of pixel. The correlation peak has been identified with the accuracy of ± 1 oversampled pixel (< 5 cm, see Table 1) and its position has given the relative offset between the corresponding azimuth lines. On the basis of this offset, each line of one of the two images has been resampled by using an 8-points cubic B-spline interpolation function, which minimises the least-square error of the function value (Strang 1986). An analysis of the techniques for oversampling SAR images and their effects on the phases can be found in Moccia et al. 1993.

Fig. 6 shows the maximum of the cross-correlation as a function of range pixels. The quadratic shape is explained by observing that the azimuth shift is proportional to the difference between the two antennas "deskew times" t_{d1} and t_{d2}, i. e. the geometrical correction necessary after having processed the raw data at $f_{DC} \neq 0$, and varying from near to far range, given by

$$t_{di} = \frac{f_{DCi}}{2\alpha_i}, \quad i = 1,2$$

where f_{DC} is the linear approximation of the Doppler centroid frequency as a function of the n-th range bin (Fig. 5), and $\alpha_i = v^2/\lambda R_{0i}$ is the azimuth chirp rate. The deskew times allow us to derive also the residual phase terms between the two images, that have to be removed before forming the interferogram.

After resampling, we multiplied one image by the complex conjugate of the co-registered image, to obtain the single-look interferogram, and successively a coherent multi-look of eight pixels in the azimuth direction was performed, in order to carry out a maximum-likelihood estimate of the phase difference (Rodriguez 1992). The eight-looks interferogram is shown in Fig. 7. The fringes are quite parallel due to the flatness of the area, and the effects on the phases of the point targets with the strongest echo returns (CRs No. 21, 23, 29, 31, with leg length of 180 cm and RCS of 41.4 dBm^2; ARC No. 1, with RCS of 44.3 dBm^2) are clearly visible.

3.2 Baseline components estimation and error budget

The next step was the estimation of the TOPSAR baseline components, which depend on the aircraft attitude dynamics. This is a crucial point when unwrapping the phases and converting the fringe map into absolute height measurements (Li and Goldstein 1990). The attitude data relative to the processed frame have been extracted from the header file
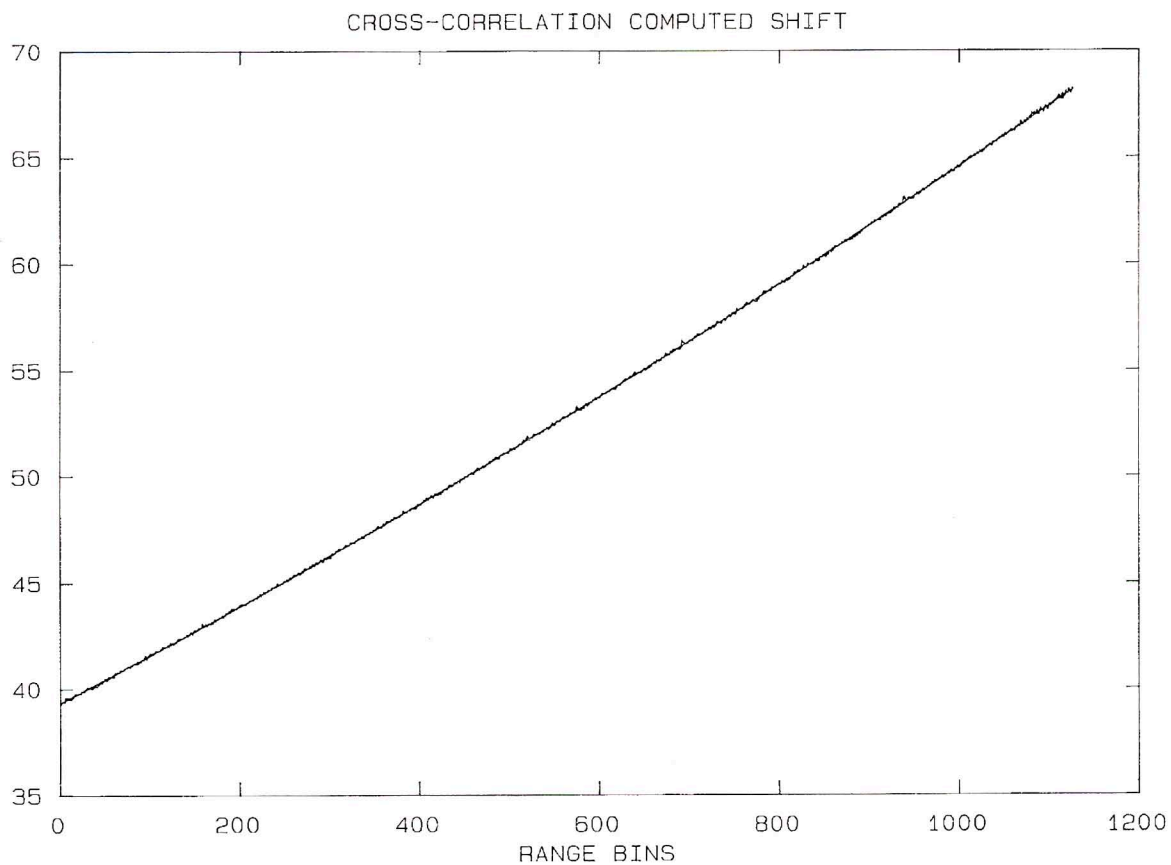
CROSS-CORRELATION COMPUTED SHIFT

Fig. 6 - Position of the peak correlation value as a function of the range bin.
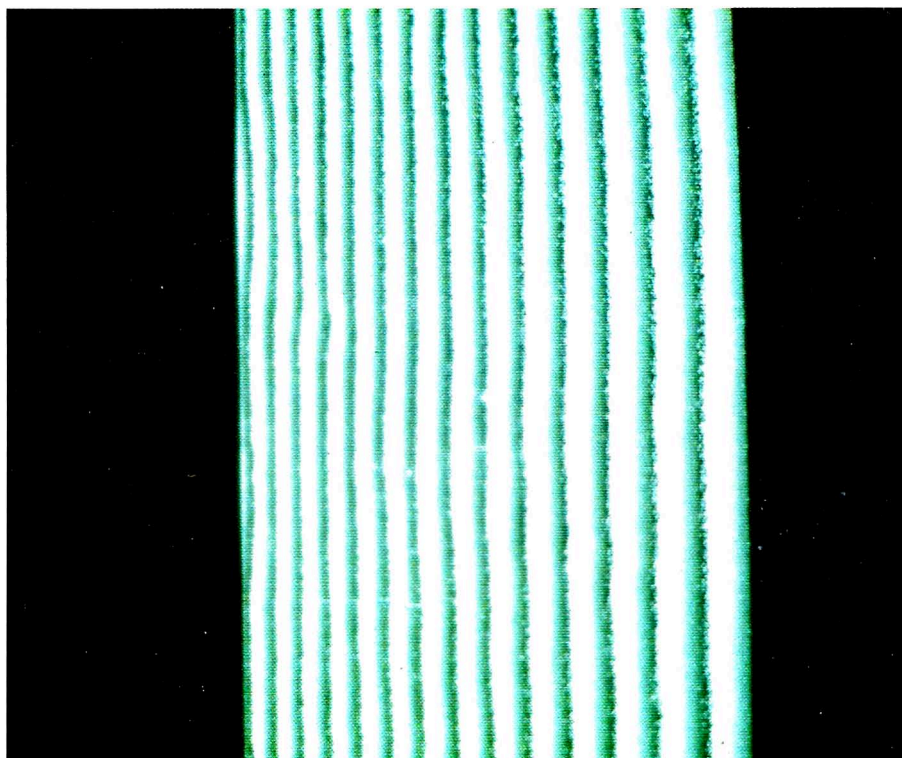

Fig. 7 - Eight-look interferogram of the processed area.

associated to the collected raw data. The ancillary information was given by the Digital Avionic Data system (DAD) and the radar inertial navigation system (LASERREF) on-board the aircraft, and it allowed us the analysis of platform motion. Fig. 8 shows the pitch, yaw and roll angles, recorded by the LASERREF system at a 50 Hz update rate, with a quantization precision of 0.01°. The yaw angle has been evaluated as the difference between the true heading and the track angle. The peak-to-peak variations of 0.25° indicate a stable flight, as also shown by the mean values and standard deviations ($\pm 1\sigma$) reported in Fig. 8. By using these average estimates, and assuming a yaw-pitch-roll rotation sequence, we applied a co-ordinate transformation to express the baseline components in a right-handed dynamic reference frame, with the origin coincident with the Inertial Navigation Unit (INU) position, the z-axis coincident with the local vertical and directed towards the Earth, and the y-axis perpendicular to the plane defined by the INU velocity vector and the local vertical (Moccia and Vetrella 1986). The reference frames are shown on Fig. 9. The transformed baseline vector (**B**) is given, in matrix notation, by M_{ypr} **B₀**, where M_{ypr} is the co-ordinate transformation matrix between the dynamic and the body-fixed reference frame (origin coincident with the INU and axes parallel to the aircraft inertia principal axes x_0, y_0, z_0), given by:

$$M_{ypr} = \begin{vmatrix} \cos\beta\cos\gamma & -\cos\alpha\sin\gamma + \sin\alpha\sin\beta\cos\gamma & \sin\alpha\sin\gamma + \cos\alpha\sin\beta\cos\gamma \\ \cos\beta\sin\gamma & \cos\alpha\cos\gamma + \sin\alpha\sin\beta\sin\gamma & -\sin\alpha\cos\gamma + \cos\alpha\sin\beta\sin\gamma \\ -\sin\beta & \sin\alpha\cos\beta & \cos\alpha\cos\beta \end{vmatrix} \quad (1)$$

where α, β and γ are the roll, pitch and yaw angles, respectively, and $\mathbf{B_0} \equiv (B_{0x}, B_{0y}, B_{0z})$ is the baseline vector in the body-fixed reference frame. Table 2a reports the lever arms, i. e. the nominal antennas' positions with respect to the body-fixed reference frame.

Assuming uncorrelated fluctuations in the observations of the attitude angles, and using Eq. (1), under the hypothesis of small angles, we obtained the following expression for the variances of the baseline components in the dynamic reference frame, $\sigma^2_{B_x}$, σ_{B_y}, $\sigma^2_{B_z}$, as a function of the variances of the estimate of the attitude angles, σ^2_α, σ^2_β, σ^2_γ, which depend on the LASERREF quantization error:

$$\begin{vmatrix} \sigma^2_{B_x} \\ \sigma^2_{B_y} \\ \sigma^2_{B_x} \end{vmatrix} \cong \begin{vmatrix} 0 & B^2_{z_0} & B^2_{y_0} \\ B^2_{z_0} & 0 & B^2_{x_0} \\ B^2_{y_0} & B^2_{x_0} & 0 \end{vmatrix} \begin{vmatrix} \sigma^2_\alpha \\ \sigma^2_\beta \\ \sigma^2_\gamma \end{vmatrix}$$

where $B_{x0} = x_{02} - x_{01}$, $B_{y0} = y_{02} - y_{01}$ and $B_{z0} = z_{02} - z_{01}$, are the nominal baseline components (see Table 2). The variances σ^2_α, σ^2_β, σ^2_γ are due to the LASERREF quantiza-
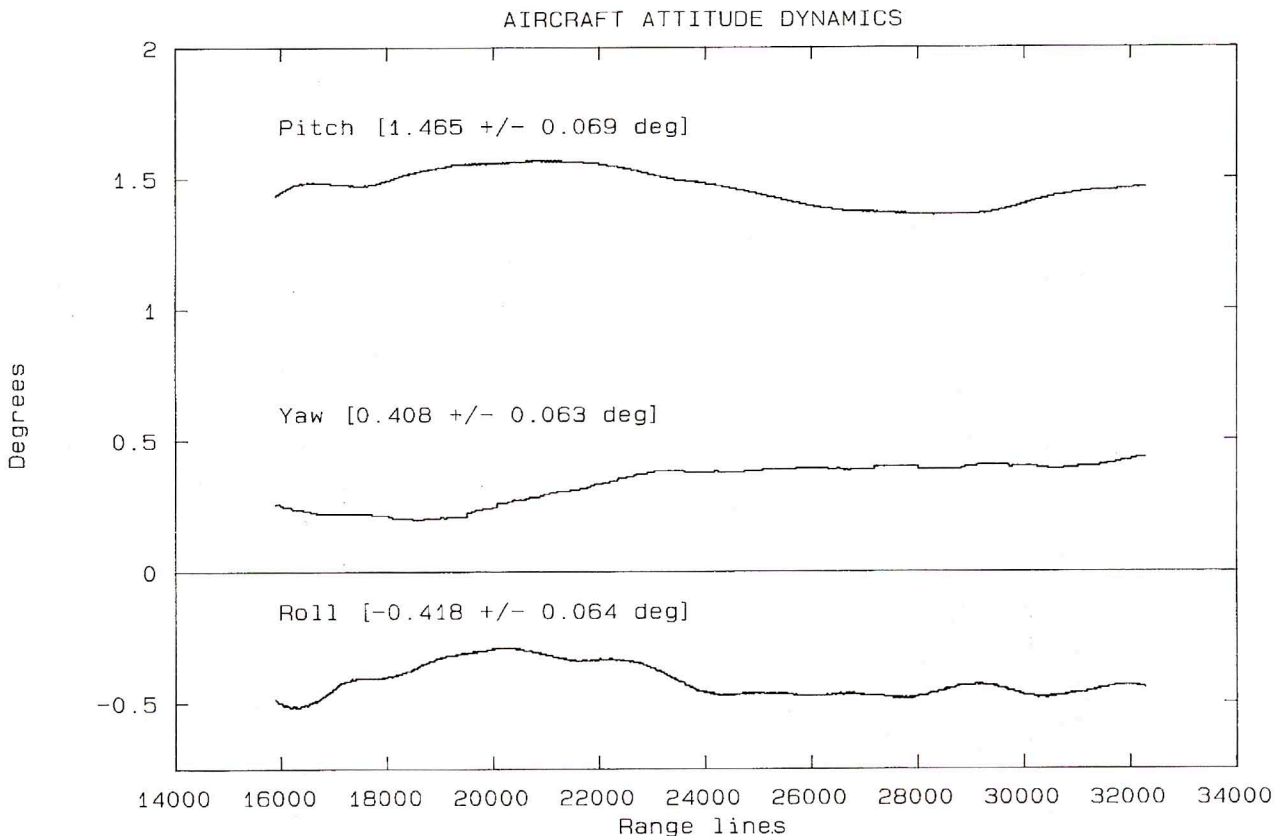

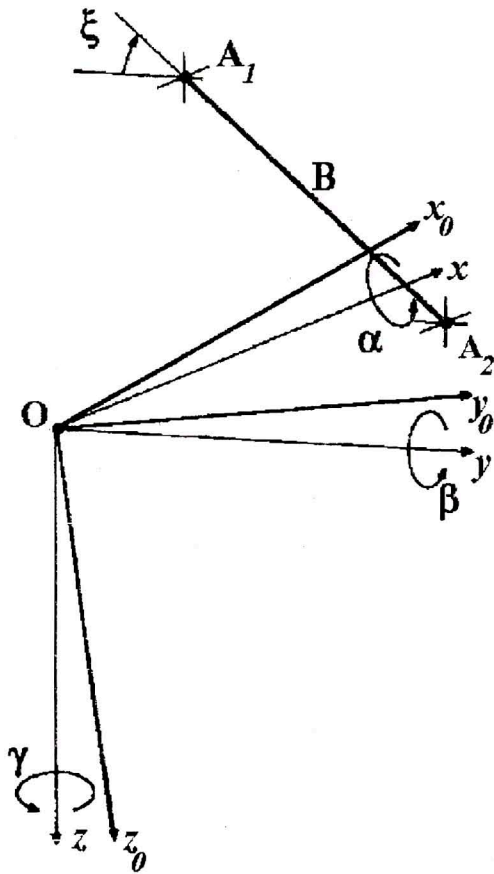*Fig. 8 - Aircraft attitude angles relative to the processed frame.*

Fig. 9 - INU-fixed and dynamic reference frames.

tion precision and are of the order of 10^{-8} rad^2. With these values, the accuracy of the baseline components estimation was of the order of ± 0.2 mm. As it will be shown in 4, these uncertainties give a major contribution to the height measurement accuracy.

3.3 Two-dimensional phase unwrapping and dem generation

The estimated baseline components (Table 2b) have been used to extract from the interferogram the information on terrain elevation. After having chosen one of the deployed calibrators (CR No. 2) as a GCP of known height, the 2π ambiguity has been solved, and the integration of the phase difference (phase unwrapping) has been carried out. We implemented a procedure based on edge detection techniques to locate the fringe lines in the interferogram (Lin *et al.* 1992), an effective method which solved satisfactorily the phase indetermination problem. In Fig. 10 the original interferogram with the edge-enhanced fringe lines, i. e. the boundaries of the 2π-addition on the integrated phase, is shown. The original fringe amplitudes and the edge-enhanced fringe contrast from near to far range are plotted in Fig. 11. As the 2π-crossing lines passed only a few nonedge points, that is, the wrong identifications of the 2π-to-0 crossings were very limited because the fringes were well
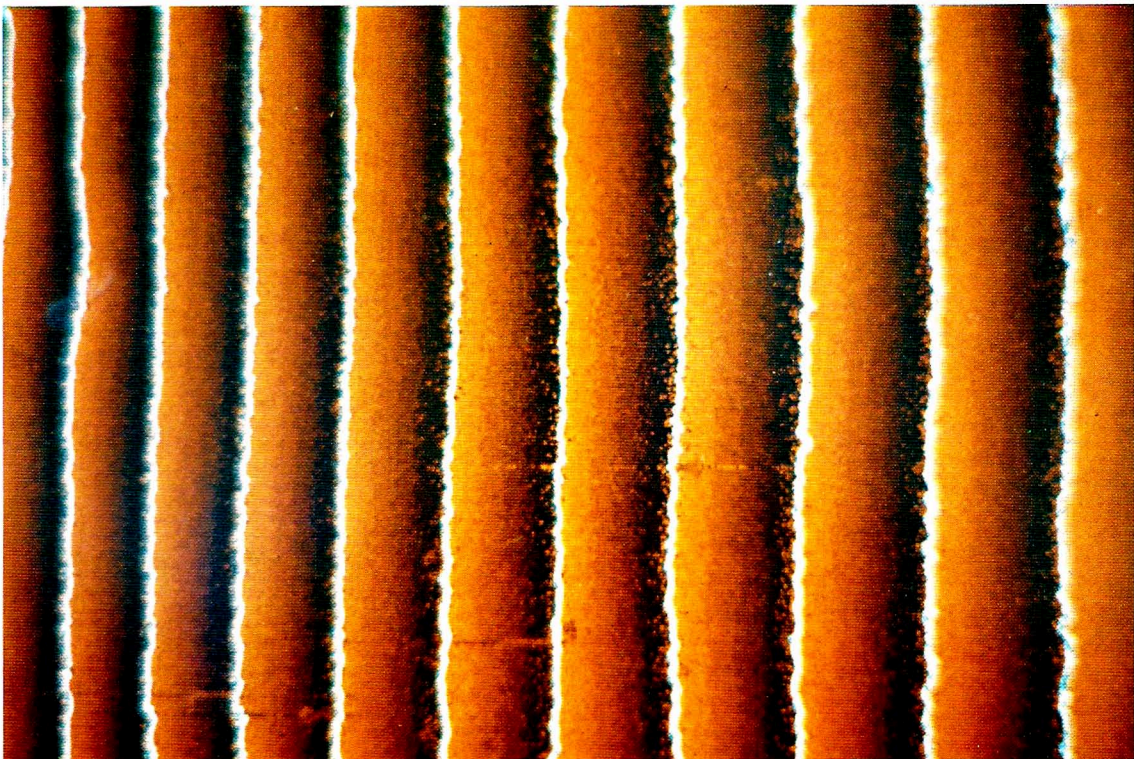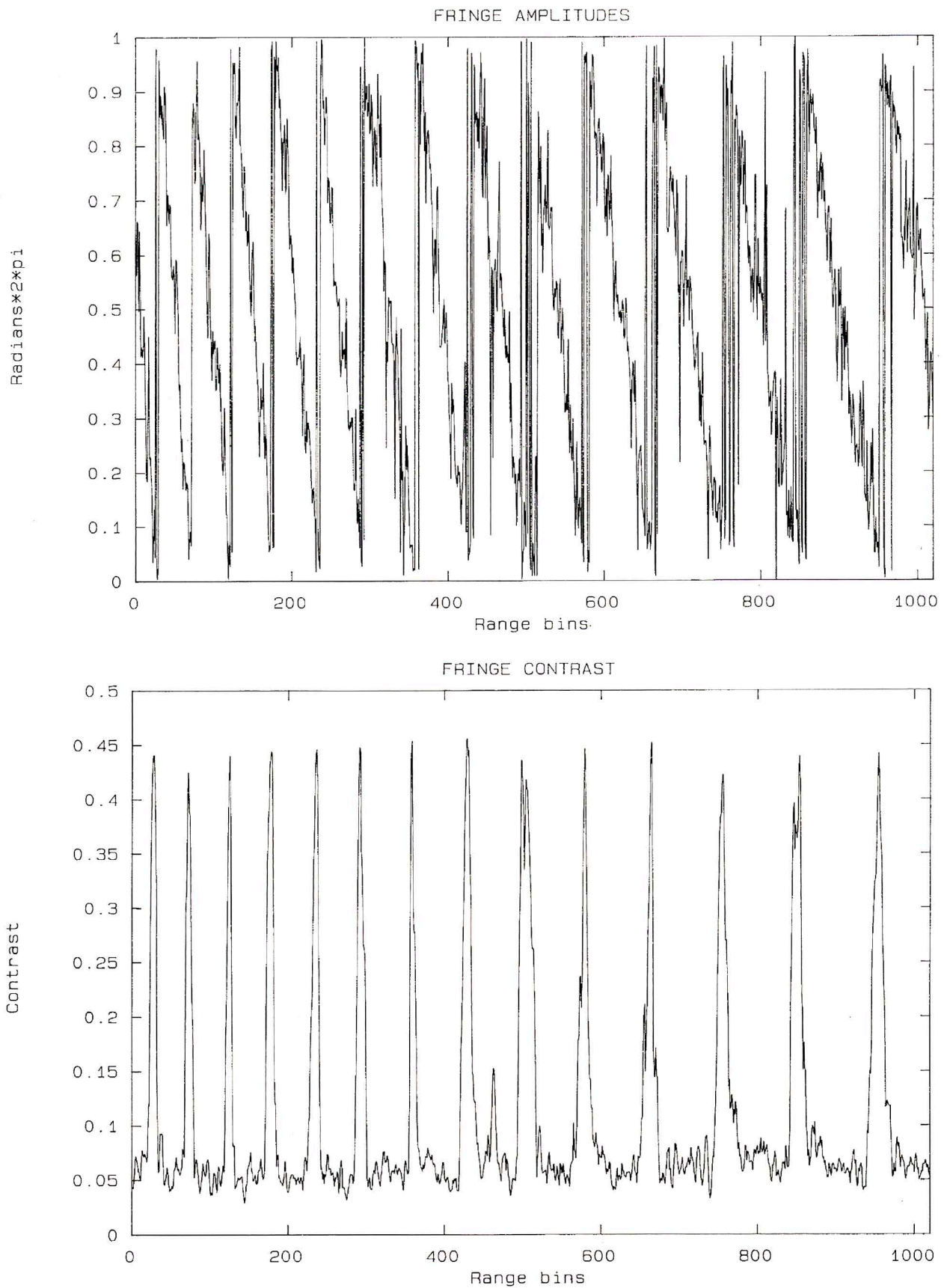

Fig. 10 - Edge-enhanced fringe lines.

Fig. 11 - Fringe amplitudes of the original 8-look interferogram (a) and fringe contrast after edge enhancement (b), from near to far range.

Table 2 - Antenna lever arms in the INU-fixed reference frame (a) and estimated baseline components in the dynamic reference frame, compared to the nominal components (b).

	x_0 [m]	y_0 [m]	z_0 [m]
A_1	2.032	–0.0785	0.6558
A_2	2.032	–1.2606	–1.6411

(a)

	Nominal	Estimated
$|B|$	2.5823 m
B_x	x_{02}-x_{01}=0.000 m	x_2-x_1=0.0541 m
B_y	y_{02}-y_{01}=–1.1821 m	y_2-y_1=–1.1991 m
B_z	z_{02}-z_{01}=–2.2969 m	z_2-z_1=–2.2876 m
Tilt angle (ξ)	62.77°	62.34°

(b)

defined, the unwrapping algorithm has worked very well, and there were little or no mislocations of fringe lines due to phase noise. In addition, the degree of coherence between the two images and the SNR were very high, and the number of residue regions (areas of inconsistent phase unwrapping) was negligible. At this point, by using the computed baseline components and the unwrapped phase information, we were able to derive a DEM. The height h of a pixel has been computed with the following equation (derived assuming a local flat Earth model):

$$h = H - R \cos \vartheta$$

where R is the slant range to the pixel, evaluated with respect to the slant range of the GCP. The look angle was evaluated from the estimated phase difference $\Delta \phi$ and the baseline tilt angle ξ by inverting the following equation:

$$\Delta \phi = \frac{2\pi}{\lambda} \left[\frac{B_{yz}^2}{2R} \sin^2(\xi - \vartheta) + B_{yz} \sin(\xi - \vartheta) - \frac{B_{yz}^2}{2R} \right] \quad (2)$$

where $B_{yz}^2 = B_y^2 + B_z^2$ is the projection of the baseline vector on the y-z plane. The residual phase term correction, described in 3.1, allows us to consider a broadside system, and to use Eq. (2) as a suitable approximation of the general equation:

$$\Delta \phi = \frac{2\pi}{\lambda} (R_1 - R_2) = \frac{2\pi}{\lambda} \frac{2\mathbf{R}_1 \cdot \mathbf{B} - B^2}{R_1 + R_2}$$

where R_1, R_2 are the moduli of the distances from the two antennas to the target.

It is worth noting that the detection of fringe lines with edge enhancement techniques was insensitive to the effect on the phases of the strongest point targets. The null line detection and the consequent unwrapping were correctly performed, whereas a first attempt of solving the 2π ambiguity, based on the identification of residues and the creation of branch cuts to identify areas of inconsistency of the phase integration (Goldstein *et al.* 1988), had shown an unacceptable error propagation in the pixel regions located near the strong point target calibrators.

As a final remark, we observe that a refinement in height evaluation can be obtained by using the INU co-ordinates: by double integration of along-track, cross-track and Earth vertical accelerations as functions of time, it is possible to compute the INU state vector with respect to an Earth-fixed right-handed reference frame. At this stage of the research activity, this technique has not been applied, because the INU vertical acceleration is invalid: further work is required to subtract the bias term from this value, and to derive the correct altitude by correlating GPS-derived data and/or barometric altitude with the "raw" vertical position given by the integrated INU data (Madsen *et al.* 1993a).

4. THEORETICAL ERROR BUDGETS ON THE HEIGHT ESTIMATE

This section briefly outlines the approach followed for a theoretical evaluation of the contributions of various error sources in the estimation of the pixel elevation. The principal error-affected parameters identified in this theoretical analysis are the aircraft altitude, the slant range knowledge, the estimated look angle, and the baseline components. Further details can be found in Li and Goldstein 1990.

4.1 Point targets

Deriving an error budget of the height estimate when the imaged pixel is representative of the echo return of a point target is useful for system transfer function evaluation (Moccia and Vetrella 1992). Fig. 12 depicts the geometry of airborne SAR Interferometry under the assumption of a flat Earth. Considering only the strong received phasor with no decorrelation effects, if h is the pixel elevation, and $\Delta \phi$ is the estimated phase difference between two homologous pixels (Eq. (2)), the basic equations for computing the topographic information are (broadside Interferometric SAR system):

$$\begin{cases} \Delta R = \dfrac{\lambda}{2\pi}\,\Delta\phi = \dfrac{B_{yz}^2}{2R}\sin^2(\xi-\vartheta) + B_{yz}\sin(\xi-\vartheta) - \dfrac{B^2}{2R} \\[2ex] h = H - R\cos\vartheta = H - R(\sqrt{1-\beta^2}\cos\xi - \beta\sin\xi) \\[2ex] \beta = \sin(\xi-\vartheta) = \dfrac{(R+\Delta R)^2 - R^2 - B^2}{2RB} \end{cases}$$

where ΔR is the path difference. Assuming uncorrelated parameters, the height measurement uncertainty σ_h^2 is (Li and Goldstein 1990):

$$\sigma_h^2 = \left(\frac{\partial h}{\partial H}\right)^2 \sigma_H^2 + \left(\frac{\partial h}{\partial R}\right)^2 \sigma_R^2 + \left(\frac{\partial h}{\partial \vartheta}\right)^2 \sigma_\vartheta^2 + \left(\frac{\partial h}{\partial B_x}\right)^2 \sigma_{B_x}^2 +$$
$$+ \left(\frac{\partial h}{\partial B_y}\right)^2 \sigma_{B_y}^2 + \left(\frac{\partial h}{\partial B_z}\right)^2 \sigma_{B_z}^2 \tag{3}$$

where:

$$\frac{\partial h}{\partial H} = 1$$

$$\frac{\partial h}{\partial R} = -\cos\vartheta$$

$$\frac{\partial h}{\partial \vartheta} = R\sin\vartheta$$

$$\frac{\partial h}{\partial B_x} = -\frac{1}{q}B_x\sin\vartheta$$

$$\frac{\partial h}{\partial B_y} = \frac{p}{q}B_y\sin\vartheta$$

$$\frac{\partial h}{\partial B_z} = \frac{p}{q}B_z\sin\vartheta$$

$$p = \frac{R}{B_{yz}}\sin(\xi-\vartheta) - \cos^2(\xi-\vartheta)$$

$$q = B_{yz}\cos(\xi-\vartheta)\left[1 + \frac{B_{yz}}{R}\sin(\xi-\vartheta)\right]$$

σ_H is the aircraft altitude uncertainty, σ_R represents the uncertainty in the sampling time of the echo return (it is of centimetric order because it depends on the SAR internal reference clock accuracy; in fact in SAR Interferometry R is not the range to be estimated, as in conventional altimeters, but it represents the sampling time of the compressed return signal), σ_ϑ is the uncertainty on the look angle, and σ_{Bx}, σ_{By}, σ_{Bz} are the baseline components uncertainties, derived from the aircraft attitude dynamics. The uncertainty on the measured phase difference, which induces an uncertainty σ_ϑ on the measured look angle, is equal to $\sqrt{SNR^{-1} + \sigma_q^2}$, where σ_q^2 is the variance of the quantization error on $\Delta\phi$. Expressing σ_h^2 as a function of the baseline length, we derived a quadratic form:

$$\sigma_h^2 = K + C\left[\frac{R\tan(\xi-\vartheta) - B\cos(\xi-\vartheta)}{RB + B^2\sin(\xi-\vartheta)}\right]^2 \tag{4}$$

where:
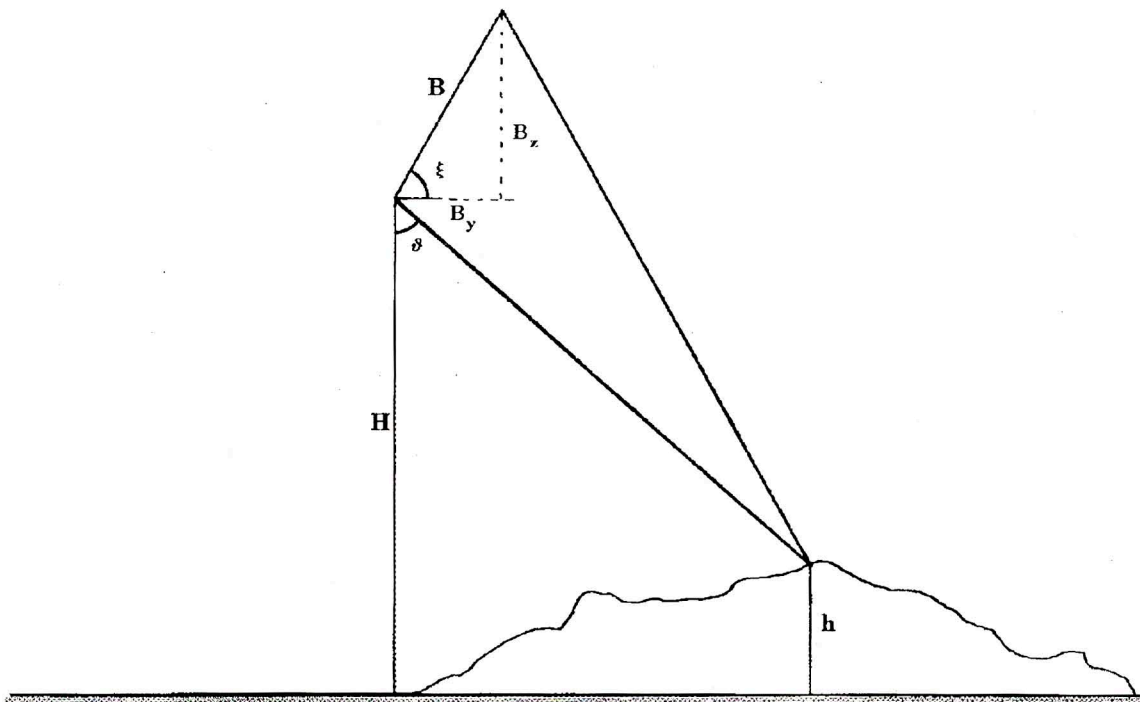

Fig. 12 - Interferometric SAR geometry (flat Earth assumption).

$$K = \sigma_h^2 + \cos^2 \vartheta \, \sigma_R^2 + R^2 \sin^2 \vartheta \, \sigma_\vartheta^2$$

$$C = R^2 \sin^2 \vartheta \, \sigma_B^2$$

and the height measurement uncertainty due to the uncertainty on B_x, of the order of 10^{-4}, has been neglected with respect to the contribution due to the uncertainties σ_{By} and σ_{Bz} ($O(10^1)$). Consequently, Eq (4) has been derived assuming $B \cong B_{yz}$. It must be pointed out that this error budget does not take the aircraft trajectory into account. In other words, we suppose that the platform centre of mass moved along a straight line, and no phase errors were induced by deviations of the flight trajectory from the linear and constant velocity motion.

4.2 Distribut targets

For a distributed target of backscattering coefficient $\sigma^0 (x, y, z)$, viewed at an incidence angle ϑ, it can be shown (Rodriguez and Martin 1992) that γ, the correlation coefficient between the interferometric echo returns v_1 and v_2, is given by:

$$\gamma = \frac{|\langle v_1 v_2^* \rangle|}{\sqrt{\langle |v_1|^2 \rangle \langle |v_2|^2 \rangle}} = \frac{|\alpha|}{1 + R_{SN}^{-1}}$$

where:

$$R_{SN} = A \, \frac{\sigma^0 \sin\vartheta \cdot \rho_{sr} \rho_{az}}{N}$$

$$|\alpha| = \left(1 - \frac{\rho_{az} B_x}{R_0 \lambda} \right) \left(1 - \frac{\rho_{sr} B_y}{R_0 \lambda \sin\vartheta} \right) \cdot$$

$$\cdot \, w \left[\frac{\delta_x}{\rho_{az}} \left(1 - \frac{\rho_{az} B_x}{R_0 \lambda} \right), \frac{\delta_r}{\rho_{sr}} \left(1 - \frac{\rho_{sr} B_y}{R_0 \lambda \sin\vartheta} \right) \right] \cdot$$

$$\cdot \, \frac{F \{ \sigma^0 \}_{(x,y,a)}}{\sigma^0 (x, y, z)}$$

$$a = - \frac{B \cos(\xi - \vartheta)}{R_0 \lambda \sin\vartheta}$$

R_{SN} is the system signal-to-noise ratio, N is the noise power (in Watts), A is a coefficient which depends on the system parameters, B_x and B_y are the along-track and cross-track baseline components, respectively, δ_x and δ_y are the azimuth and range offsets between the two images, $w(x, y)$ is the impulse response function, which has been chosen to be given by a two-dimensional *sinc* function. The operator $F \{ \bullet \}$ represents the Fourier transform of σ^0, evaluated in

(x, y, a). The uncertainty on the phase difference, $\sigma_{\Delta\phi}$, is derived by applying the Cramer-Rao bound on the estimator of $\Delta\phi$ from an N_L-looks image (Rodriguez 1992):

$$\sigma_{\Delta\phi}^2 = \frac{1}{2N_L} \frac{1 - \gamma^2}{\gamma^2}$$

to be applied in Eq. (3) to derive the height error budget for distributed targets. A plot of Eq. (4) is shown in Fig. 13, obtained using a value of ± 0.2 mm for the uncertainty on the baseline components, ± 1 m for the uncertainty on aircraft altitude, and with 45° incidence angle (mid swath). Considering our baseline length of 2.58 m, and without motion compensation, the expected height error is ± 4.5 m for point targets and ± 2.7 m for extended targets. The SNR values adopted are 18 dB for point targets, and 13 dB for extended targets, whereas the standard deviation of the quantization error, σ_q, was set to $1.7 \cdot 10^{-4}/\sqrt{12}\, radians$.

5. DEM VALIDATION

The DEM of the area under study, after the removal of systematic errors by using the known GCP's height, was evaluated by performing a comparison with the digitised scattered height-points sampled by IGMI. The IGMI height points have an accuracy of ± 3 m at 1:25,000 scale. The DEM in raster format was obtained from the original elevation points by means of a computer code (Vetrella and Moccia 1988). Currently, no rectification of the radar-derived height map has been implemented, and studies on co-registration between radar DEMs and reference DEMs are being performed. Nevertheless, it has been possible to verify the quality of the height map obtained by means of interferometry, on the basis of the knowledge of elevation and position of the CRs and ARCs deployed on the test-site. We chose fifteen CRs to carry out an analysis of the difference between the true height value and the computed elevation: the root-mean-square value of this difference has been found to be about 15 m, which is about 200% greater than the predicted theoretical value (see Fig. 13). Table 3 shows the height values in both cases, from the radar-derived map and from the reference DEM.

In order to make use of extended targets in the validation of our DEM, we cut eight areas of 15x15 pixels (i. e., about 2,000 m^2), large enough to be considered representative of a distributed target, and sufficiently small to assume the incidence angle constant over the whole region. The analysis of the rms difference gave us an estimate of the rms height error for uniform areas. The cuts were close to the positions of the selected CRs, but without including their responses, and they have been chosen and located on the IGMI DEM
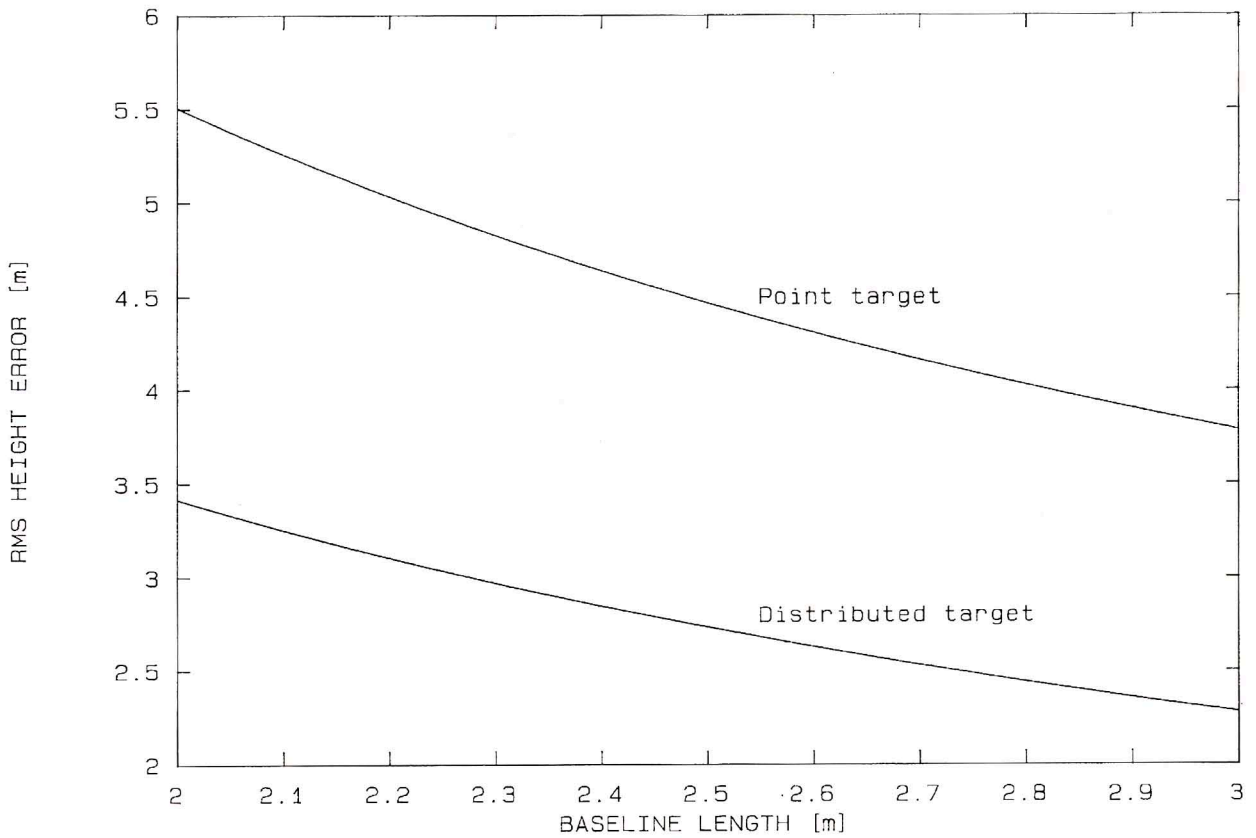
Fig. 13 - Theoretical error budget on the height estimate.

as flat areas. From the results shown on Table 4, the mean rms value of the difference between true and computed heights is ± 8.1 m, about 200% greater than the theoretical error budget.

Table 3 - Rms height difference for 15 point targets.

CR #	True height [m]	Computed height [m]
2	394.22	403.09
5	385.19	399.04
8	377.56	390.29
9	376.67	384.81
10	378.18	391.51
11	379.49	384.24
12	377.51	359.56
13	378.96	386.57
15	380.62	366.30
16	385.93	398.33
18	385.54	356.15
21	401.80	403.38
23	400.16	379.86
31	389.08	391.58
40	393.19	368.74

Root mean square error [m]	14.7

Table 4 - Rms error for eight homogeneous areas (extended targets).

Area #	Mean altitude [m] 15x15 pixel avg	rmse [m] 15x15 pixel avg
5	392	7.4
8	388	8.0
10	388	9.0
11	387	7.7
12	386	8.1
15	390	8.3
31	391	7.8
40	397	8.8

CONCLUSIONS AND FUTURE ACTIVITIES

We have presented the analysis and the main results of the TOPSAR experiments conducted in 1991 in Southern Italy, devoted to assess the TOPSAR capability to produce high-quality DEMs. By using a SAR processor developed by CO.RI.S.T.A., the interferometric raw data collected by the two channels have been focused separately, and an interferogram of an area on which several point targets were deployed has been derived. After co-registration of the images, which had a relative squint angle of 0.2, we estimated the baseline time-varying components from the header data relative to the processed frame, and we performed a fringe-enhancement procedure by means of edge detection algorithms to correctly unwrap the phase information. The DEM obtained from the XTI SAR data has been validated by computing the height rms error with respect to the IGMI digitised elevation points of the test site. This procedure has been applied to a set of homogeneous areas, as well as to a set of 15 point targets, which height was known after a ground truth campaign. The theoretical error analysis for both point and extended targets have shown rms values of the height accuracy less than the values found on the TOPSAR DEM.

The primary improvement to be performed in our interferometric processing is the development of a more sophisticated motion compensation algorithm. With a very accurate knowledge of aircraft position, velocity and attitude, it will be possible to estimate and remove the additional error contributions to the interferometric phase due to motion of the platform. In addition, the atmospheric corrections seem to play an important role in the absolute accuracy requirements (Madsen *et al.* 1993b), together with the need of state-of-the-art reference DEMs, in order to perform the phase calibration of a SAR interferometer, and to validate motion compensation algorithms. Work is currently underway in "de-biasing" the on-board INU data relative to vertical accelerations and position, to obtain correct reference terms which could improve the phase unwrapping technique, by means of a better knowledge of the altitude. As a by-product, it will be possible to refine the evaluation of the baseline components, as outlined in § 3.2.

A further promising motion compensation technique that we are presently analysing consists in the determination of the aircraft trajectory and altitude by making use of the phase histories of the point targets. In this case, the time-varying antenna-target distances allow one to compute the antenna position and velocity vector components in an Earth-fixed reference frame, by using least squares approximations. Of course, this technique has its major limitation in the availability of strong and precisely located point targets within the area under study. Nevertheless, it can be used to validate

and/or integrate on-board ancillary data, giving results which can be extrapolated to the whole trajectory.

Finally, further activity is required in order to implement co-registration techniques between available reference DEMs, converted to raster format, and interferometric DEMs, either by using arrays of corner reflectors, as done by Madsen *et al.* 1993 with the TOPSAR data sets gathered during the 1992 experiments at Ft. Irwin, or by estimating geometric distortions such as misalignment, skew or slope errors. An airborne interferometric SAR simulator, which is currently being developed and tested, could be a useful tool in studying, evaluating and simulating sensor errors, target mislocation, foreshortening and layover effects, and processor-induced geometric distortions. The main objective is an automated procedure to map the SAR image into a rectified, ground-range format, compensated for terrain and processing effects.

REFERENCES

CO.RI.S.T.A., 1991, *Progetto SAR 1991: Rapporto Finale Campagna Agrisar*. A report prepared by AQUATER SpA. CO.RI.S.T.A. internal document 004/92.

Curlander, J. C., and McDonough, R. N., 1991, *Synthetic Aperture Radar*. Systems and Signal Processing (New York: John Wiley & Sons, Inc.).

Gabriel, A. K, and Goldstein, R. M., 1988, *Crossed orbit interferometry: theory and experimental results from SIR-B*. International Journal of Remote Sensing, Vol. 9, No. 8, pp.857-872.

Goldstein, R. M., Zebker, H. A., and Werner, C. L., 1988, *Satellite radar interferometry: two-dimensional phase unwrapping*. Radio Science, Vol. 23, No. 4, pp. 713-720.

Graham, L. C., 1974, *Synthetic Interferometer Radar For Topographic Mapping*. Proceedings of the IEEE, Vol. 62, No. 6, pp. 763-768.

Gray, A. L., Farris-Manning, P. J., 1993, *Repeat-Pass Interferometry with Airborne Synthetic Aperture Radar*. IEEE Transactions on Geoscience and Remote Sensing, Vol. 31, No. 1, pp. 180-191.

JPL SIR-C Team, DLR NE-HF X-SAR Team, I-PAF X-SAR Team, 1990, *Data products and image quality assessment for the SIR-C/X-SAR mission*, Version 1.0. JPL Document D-7193.

Li, F. K., Held, D. N., Curlander, J. C., and Wu, C., 1985, *Doppler Parameter Estimation for Spaceborne Synthetic-Aperture*

Radars. IEEE Transactions on Geoscience and Remote Sensing, Vol. GE-23, No. 1, pp. 47-56.

Li, F. K., and Goldstein, R. M., 1990, *Studies of Multibaseline Spaceborne Interferometric Synthetic Aperture Radars.* IEEE Transactions on Geoscience and Remote Sensing, Vol. 28, No. 1, pp. 88-97.

Lin, Q., Vesecky, J. F., Zebker, H. A., 1992, *New Approaches in Interferometric SAR Data Processing.* IEEE Transactions on Geoscience and Remote Sensing, Vol. 30, No. 3, pp. 560-567.

Madsen, S. N., Zebker, H. A., Martin, J., 1993a, *Topographic Mapping Using Radar Interferometry: Processing Techniques.* IEEE Transactions on Geoscience and Remote Sensing, Vol. 31, No. 1, pp. 246-256.

Madsen, S. N., Martin, J., and Zebker, H. A., 1993b, *Analysis and Evaluation of the Performance of the TOPSAR Interferometer, EARSeL/CO.RI.S.T.A.* International Workshop on SAR Interferometry, Naples, May 18-20 1993

Moccia, A., Esposito, S., and D'Errico, M., 1993, *Height Measurement Accuracy of ERS-1 SAR Interferometry, EARSeL/CO.RI.S.T.A.* International Workshop on SAR Interferometry, Naples, May 18-20 1993.

Moccia, A., Vetrella, S., 1986, *An integrated approach to geometric precision processing of spaceborne high-resolution sensors.* International Journal of Remote Sensing, Vol. 7, No. 3, pp. 349-359.

Moccia, A., and Vetrella, S., 1992, *A Tethered Interferometric Synthetic Aperture Radar (SAR) for a Topographic Mission.* IEEE Transactions on Geoscience and Remote Sensing, Vol. 30, No. 1, pp. 103-109.

Moccia, A. Vetrella, S., and Ponte, S., 1991, *Passive and Active Calibrators Characterization by Using a Spaceborne SAR System Simulator.* Proc. of the SAR Calibration Workshop held at DLR, Oberpfaffenhofen, October 9th-11th, 1991. Accepted for publication on IEEE Transactions on Geoscience and Remote Sensing, 1993.

Prati, C., Rocca, F., Monti Guarnieri, A., and Damonti, E., 1990, *Seismic Migration for SAR Focusing: Interferometrical Applications.* IEEE Transactions on Geoscience and Remote Sensing, Vol. 28, No. 4, pp. 627-640.

Rodriguez E., 1992, *Maximum likelihood estimation of the interferometric phase from distributed targets.* IEEE Transactions on Geoscience and Remote Sensing, to be published.

Rodriguez, E., Martin, J. M., 1992, *Theory and design of interferometric synthetic aperture radars.* IEE Proceedings, Vol. 139, No. 2, pp. 147-159.

Strang, G., 1986, *Introduction to applied mathematics* (Wellesley-Cambridge Press, Wellesley, MA), pp. 177-180.

Vetrella, S., and Moccia, A., 1988, *A Procedure for Modeling the Terrain Relief by Using Digitized Topographic Maps.* Geocarto international, Vol. 3, No. 3, pp. 3-11.

Zebker, H. A., Madsen, S. N., Martin, J., Wheeler, K. B., Miller, T., and Lou, Y., Alberti, G., Vetrella, S. and Cucci, A., 1992, *The TOPSAR Interferometric Radar Topographic Mapping Instrument.* IEEE Transactions on Geoscience and Remote Sensing, Vol. 30, No. 5, pp. 933-940.

Zebker, H. A., and Goldstein, R. M., 1986, *Topographic Mapping From Interferometric Synthetic Aperture Radar Observations.* Journal of Geophysical Research, Vol. 91, No. B5, pp. 4993-4999.